Journal of Materials Chemistry B

Accepted Manuscript

ROYAL SOCIETY OF CHEMISTRY

www.rsc.org/materialsB

Synthesis, characterization and formation mechanism of magnesium- and strontium-substituted hydroxyapatite

Zhen Geng[a], Zhenduo Cui[a], Zhaoyang Li[a,b,*1], Shengli Zhu[a,b], Yanqin Liang[a], William Weijia Lu[c], Xianjin Yang[a,b,*2]

[a]School of Materials Science and Engineering, Tianjin University, Tianjin 300072, China

[b]Tianjin Key Laboratory of Composite and Functional Materials, Tianjin 300072, China

[c]Department of Orthopaedics & Traumatology, The University of Hong Kong, Hong Kong, China

Abstract

Magnesium (Mg) and strontium (Sr) have been widely used in the field of implanted devices because of their excellent bioactivity. However, the local high ion concentration caused by the implant affects the growth of hydroxyapatite ($Ca_{10}(PO_4)_6(OH)_2$, HA), which is the main inorganic component of bone and teeth. Many studies have investigated the effect of Mg^{2+} and Sr^{2+} on the growth of HA, but no systematic research has been conducted to compare these two ions in terms of the growth of HA. In this study, the substitution of a series of Sr- and Mg-substituted HA was conducted through a conventional hydrothermal method. Comprehensive characterization techniques, including X-ray diffraction, inductive coupled plasma, field emission scanning electron microscopy, transmission electron microscopy,

*Corresponding author at: School of Materials Science and Engineering, Tianjin University, 92 Weijin Road, Tianjin 300072, China. Tel.: +86 022 27402494. Fax.: +86 022 27402494.
E-mail address: zyli@tju.edu.cn (Z.Y. Li).

*Corresponding author at: School of Materials Science and Engineering, Tianjin University, 92 Weijin Road, Tianjin 300072, China. Tel.: +86 022 27402494. Fax.: +86 022 27402494.
E-mail address: xjyang@tju.edu.cn (X.J. Yang).

selected-area electron diffraction, thermo gravimetric-differential scanning calorimetry, and Fourier transform infrared spectroscopy, were used to examine the effects of Sr^{2+} and Mg^{2+} on the phase, morphology, crystallinity, chemical composition, thermal stability, and lattice parameters of HA. The results indicated that Mg ions partially substituted for calcium (Ca) ions in the apatite structure, thus decreasing the lattice parameters, partially adsorbing on the apatite surface that formed the amorphous phase, and inhibiting the crystal growth. By contrast, Sr ions fully substituted for Ca ions and increased the lattice parameters. Both Mg and Sr ions affected the morphology of HA. Crystallinity decreased with the addition of Mg ions (transition from crystal to amorphous phase was between 30% and 40% Mg), but it was not affected by Sr ions. Thermostability decreased with the addition of Mg (a total weight loss from 8.06 wt.% for 10% Mg to 25.81 wt.% for 50% Mg), but it had no significant changes in the Sr-substituted samples.

Key words: Hydroxyapatite, Magnesium, Strontium, Crystallinity, Lattice parameter.

1. Introduction

Since the first report on HA [1], which is the main mineral component of bone tissue and teeth, it has been widely used for biomedical applications because of its excellent bioactive, biocompatible, and osteoconductivity properties in human body constituents [2-5]. However, the in vivo degradation rate of HA is slow compared with the fast growth rate of newly formed bone [6]. Therefore, improving the ability of HA degradation is necessary. So far, many techniques have been used to increase the degradation rate of HA, such as reducing the atom ratio of calcium (Ca) to

phosphorus (P) and crystallinity [7], decreasing the crystal size [8], and fabricating macropore into its structure [9], etc. One of the most effective and feasible ways of increasing the degradation rate of HA is introducing extrinsic ions into its lattice, such as F^- [10], Zn^{2+} [11], Ba^{2+} [12] and Co^{2+} [13], particularly for Mg^{2+} and Sr^{2+} [14-15].

As the main group elements with Ca, both magnesium (Mg) and strontium (Sr) have excellent biological activity [16-18]. Enamel, dentin, and bone contain 0.44, 1.23, and 0.72 wt.% of Mg, respectively [19]. Mg plays a key role in bone metabolism, particularly during the early stages of osteogenesis, in which it stimulates osteoblast proliferation and its depletion adversely affects all stages of skeletal metabolism, causing cessation of bone growth, decreases in osteoblast activity, osteopenia, and bone fragility [20-21]. Sr has been proved to be an effective anti-osteoporotic element through its anti-resorptive and bone-forming effects [22-23]. In vitro experiments showed that Sr not only enhances the proliferation of preosteoblastic cells and bone matrix synthesis but also reduces the osteoclast activity [24-27]. Sr has also been demonstrated to stimulate bone formation and decrease bone resorption in vivo [28-29]. As a kind of medicine, Strontium ranelate (SR) has a curative effect on reducing the risk of vertebral and femoral bone fractures in postmenopausal women with osteoporosis [30-31]. Despite the excellent bioactivity of Sr and Mg, their use causes local high concentrations of these ions. Boivin et al. [32-33] found that Sr in bone after SR treatment was 60 times more than the normal level. Such a high concentration of ions greatly affects the morphology, crystallinity, and growth rate of HA [32-34].

As well known, the HA structure has a C3 symmetry and contains two types of Ca atoms, namely, Ca(I) and Ca(II), which differ in their coordination and bonding properties. The Ca(I) site coordinates with phosphate oxygen only and consists of a set of three Ca atoms positioned at z = 0, 1/2, and 1 levels on the three-fold rotation axis parallel to the crystallographic c-axis. The Ca(II) site is linked to both phosphate oxygen and a hydroxyl group, and it consists of a set of six Ca atoms positioned as three by three on the mirror planes at z = 1/4 and 3/4 [35]. Many studies have been conducted on the effects of Mg or Sr on HA. It was generally accepted that the lattice parameters decreased with the addition of Mg and increased with the addition of Sr. Meanwhile, crystallites become more irregular with the increasing content of both Mg and Sr [36-37]. However, how exactly Mg- or Sr-incorporation affects the bulk structure of apatites remains unknown. Studies found that Mg or Sr could enter either the Ca(II) site [36, 38], or the Ca(I) site [39-40]. Furthermore, no systematic research has yet compared the effects of Mg^{2+} and Sr^{2+} on HA through hydrothermal method. In this study, the Mg- and Sr-substituted HA was prepared by hydrothermal method. The effects of cation substitution on the morphology, crystallinity, and growth mechanism were discussed.

2. Materials and methods

2.1. Preparation of samples

All the samples were synthesized by using a one-step hydrothermal method as previously reported [41], but with a slight modification. Briefly, $Ca(NO_3)_2 \cdot 4H_2O$, $Mg(NO_3)_2 \cdot 4H_2O$, $Sr(NO_3)_2$ and Na_3PO_4 were used as the Ca, Mg, Sr and P sources,

respectively. For pure HA nanocrystallite, $Ca(NO_3)_2 \cdot 4H_2O$ and Na_3PO_4 with a molar ratio of 10:6 were dissolved in 80 mL deionized water, respectively. Then, $Ca(NO_3)_2 \cdot 4H_2O$ solution was added dropwise into the Na_3PO_4 solution. After agitating rigorously for 10 min, the suspension was hydrothermally treated at 150 ℃ for 5 h. The precipitates were washed respectively by deionized water and dehydrated absolute ethanol twice. The product was placed in an oven and heated at 70 °C for 24 h for drying. Subsequently, the dried powder was manually ground with a corundum mortar. Sr-HA and Mg-HA nanocrystallites with different Sr and Mg contents were synthesized by replacing $Ca(NO_3)_2 \cdot 4H_2O$ with $Sr(NO_3)_2$ and $Mg(NO_3)_2 \cdot 4H_2O$, respectively. The samples were distinguished by the substitution ion concentration. For example, 10% Mg indicates that the sample has an Mg/(Ca + Mg) concentration of 10 mol.%. The Mg and Sr substitution degrees in HA are designed to vary from 10 to 100%.

2.2. Materials characterization

The atomic concentrations of the elements (Ca, Mg, Sr, and P) in the samples were quantified by inductive coupled plasma emission spectrometer (ICP, VISTA-MPX) method.

Lattice parameters (c and a) were calculated from peaks (0 0 2) and (2 1 1), respectively, using the standard HCP unit cell plane spacing relationship [42]:

$$\frac{1}{d^2} = \frac{4}{3}\left(\frac{h^2 + hk + k^2}{a^2}\right) + \frac{l^2}{c^2} \qquad (1)$$

where d is the distance between two adjacent planes in the set of Miller indices (h k l).

The crystallinity degree, corresponding to the fraction of crystalline phase present in the examined volume, was evaluated by the equation (2) [43]:

$$Xc \approx 1 - \left(V_{112/300} / I_{300}\right) \qquad (2)$$

where $\boldsymbol{I}_{300}$ is the intensity of (300) reflection and $\boldsymbol{V}_{112/300}$ is the intensity of the hollow between (112) and (300) reflections, which completely disappears in non-crystalline samples.

To examine the functional groups of the obtained powder, infrared spectra of all samples were obtained using an infrared Fourier-transform spectrometer (FT-IR, Bruker Tensor 27, Germany) in the range of 4000 cm^{-1} to 400 cm^{-1}. The powder was ground with KBr in the proportion of 1/150 (by weight) and pressed to a wafer with a diameter of 13mm using a hand press.

Phase analysis of the synthesized powders was conducted using X-ray powder diffraction (XRD). The XRD patterns were obtained using a Bruker D8 advance X-ray diffractometer equipped with graphite monochromatized Kα radiation (λ = 1.5418 Å). The diffractometer was operated at 40.0 kV and 30.0 mA at a 2θ range of 10° to 90° using a step size of 0.05 and a 50 s exposure.

The powder morphology was observed by scanning and transmission electron microscopy (FESEM; TEM). A 5 kV accelerating voltage was chosen for SEM analysis and the micrographs were captured using secondary electrons collected with an in-lens detector. TEM images were taken using a JEM-2100F microscope at 200 kV. High-resolution imaging (high-resolution transmission electron microscopy (HRTEM)) and selected-area electron diffraction (SAED) patterns were obtained.

The thermal gravimetric (TG) analysis was performed by a TGA/DSC 1 (METTLER TOLEDO, Switzerland) to analyze the thermal behavior of the powder during heating. The sample weight was 30 mg and heating was performed in an alumina crucible at a rate of 10 °C min^{-1} up to 1000 °C.

2.3 Data analysis

Dedicated software, such as DigitalMicrograph 365 (for PC) (Gatan, Inc., Pleasanton, CA) and MicroCall Origin, was used for image processing and mathematical data computation.

3. Results

3.1. Phase identification from XRD patterns

The typical XRD patterns of all synthesized samples are shown in Fig. 1. The diffraction peaks shifted to low 2θ values with the Sr addition and to high 2θ values with the Mg addition, indicating an increase (decrease) in d-spacings and hence lattice parameters. This was due to the higher ionic radius of Sr ion (1.13 Å) and the lower ionic radius of Mg ion (0.72 Å) than that of Ca ion (0.99 Å) [44]. The patterns showed that all Sr-substituted HA samples had good crystallinity. However, the peaks were dramatically broadened with the addition of Mg, indicating a decrease in crystallinity. The patterns showed a characteristic amorphous peak when the content of Mg was 50%. The moving distances of the peak position of Sr were larger than those of Mg as presented on the (002) lattice plane, indicating the greater substitution of Sr than Mg.

The cell parameters and crystallinity of the samples are shown in Table 1. The lattice parameters for both *a* and *c* evidently increased with the addition of Sr. By

contrast, both *a* and *c* considerably decreased with the substitution of Mg. The addition of Mg considerably decreased the crystallinity of HA. When the Mg content was more than 30%, no diffraction peaks were found by X-ray diffraction analysis. Although the crystallinity of HA decreased with the incorporation of Sr, it was not so significantly affected as Mg.

3.2. Chemical analysis

ICP provides the quantitative composition of the synthesized precipitates. The relative amounts of Ca, Mg, Sr, and P in the precipitates are listed in Table 2. The Mg concentrations in the precipitates were lower than those in the synthesized solutions. The values of (Ca + Mg):P decreased with the addition of Mg. However, the measured Sr contents were in good agreement with the designated Sr contents of powders. Furthermore, the values of (Ca + Sr):P were similar to those of Ca:P of pure HA. It was not surprising that HA and Mg-HA had a measured Sr content of 0.03 ~ 0.07 mol.%. Traceable Sr in water and other sources may incorporated into HA and Mg-HA during the reaction.

3.3. Functional groups

Fig. 2 shows the FT-IR spectra of the prepared samples. The IR spectra of each prepared powder were characteristic of phosphate compounds. The band at 963 cm^{-1} was attributed to the υ_1 vibration peak of PO_4^{3-}. The 472 cm^{-1} band was derived from the υ_2 phosphate mode. As a major peak of the phosphate group, the υ_3 vibration peak was observed in the region between 1000 cm^{-1} and 1100 cm^{-1}. The absorption peaks located at 577 cm^{-1} and 603 cm^{-1} were assigned to the υ_4 vibration mode of PO_4^{3-}. The

absorption bands at 875 cm^{-1} and 1640 cm^{-1} were assigned to the HPO_4^{2-} group. The absorption band at 1390 cm^{-1}, which was derived from the vibration of the CO_3^{2-} group, was attributed to the CO_2 from air. The wide absorption band observed at 3300 cm^{-1} to 3600 cm^{-1} was attributed to lattice H_2O [37]. The addition of Sr had no obvious impacts on the absorption peaks, except for the strengthening and broadening of the carbonate absorption bands. Moreover, the band intensity and the band resolution corresponding to the PO_4^{3-} vibration modes decreased with the addition of Mg. The υ_1 and υ_2 vibration peaks of PO_4^{3-} disappeared when the Mg content increased up to 50%.

3.4. SEM observation

Fig. 3 shows the morphology of HA and synthesized samples with different Mg and Sr contents. The average size of HA was around 50 nm. With the addition of Mg, the morphology of the samples changed from nanoparticles (10% Mg) to fusiform clusters with an average size of 200 nm to 400 nm (30% Mg) and was finally converted to nearly-spherical nanoparticles (50% Mg), as shown in Fig. 3 (a)-(c). The morphology of the samples added with Sr did not show significant differences with each other and HA, only a slight deformation, as shown in Fig. 3 (d)-(f).

3.5. TEM analysis

Fig. 4 shows the TEM and SAED patterns of the synthesized samples. The morphology of pure HA was regular nanoparticles with good crystallinity (Fig. 4 (a, b)). The nanoparticles became irregular with the addition of Mg up to 10% Mg-HA (Fig. 4 (c)). As shown in Fig. 4 (e), 30% Mg-HA was a fusiform cluster composed of

nano-rods, which were made up of fine nanoparticles. About 50% Mg-HA showed a nano-hollow spherical structure and formed agglomerates (Fig. 4 (g)). For Sr-HA, the morphology of the samples became irregular with the increased content of Sr (Fig. 4 (d, f, h)). Some hexagonal crystals could still be seen in the 10% Sr samples (inset of Fig. 4 (d)). However, the particles were fully irregular in 50% Sr. All these samples characterized by TEM conformed to those characterized by SEM. The SAED patterns, which agreed with the results of XRD, demonstrated all samples had good crystallinity except 50% Mg-HA.

To investigate the amorphous samples of 50% Mg-HA, the results of the measurements of elemental mapping are presented in Fig. 5. The elemental maps show a homogenous distribution of Ca, Mg and P in the structure. Therefore, the agglomerates formed by the nano-hollow sphere are confirmed to be amorphous phosphate.

The HRTEM patterns for each sample were obtained to illuminate more of the details, as shown in Fig. 6. The arrowhead represents the growth direction of the c-plane. The HA nanoparticles have good crystallinity. Both the growth of the c-plane and the crystal size were inhibited by the addition of Mg (Fig. 6 (a, b)). The degree of crystallinity was poor, as proved by XRD and SAED, when Mg content increased up to 50%. However, atoms with short-range ordering were still visible (Fig. 6 (c)). All Sr-substituted HA samples had good crystallinity, consistent with the XRD results, but the deformation degree of the samples increased with the addition of Sr (Fig. 6 (d-f)). The images also show that the (0 0 2) lattice spacing of 30% Mg and 50% Sr was

0.336 nm and 0.35nm, respectively, which is smaller (larger) than the (0 0 2) lattice spacing of HA (0.34nm), thus indicating the incorporation of the ions.

3.6. TG analysis

The TG plots illustrated in Fig. 7 show the weight loss along the investigated temperature range for the precipitated powders with different concentrations of added Mg and Sr. For Mg-HA, the total weight loss increased with the increasing Mg content and was 8.06 wt.% for 10% Mg, 14.97 wt.% for 30% Mg and 25.81 wt.% for 50% Mg. Significant loss of weight up to approximately 400 °C was due to the loss of adsorbed (up to 200 °C) and lattice water [45]. Loss of the carbonate ions could be attributed to the total weight loss above 550 °C [22]. HPO_4^{2-} groups, which could account for the weight loss in the temperature range of 400 °C to 700 °C, were incorporated into the HA lattice with a water formation according to the following reaction: $2\ HPO_4^{2-} \rightarrow P_2O_7^{4-} + H_2O$ [45]. The sharp weight loss of 50% Mg in this range indicated that it had higher HPO_4^{2-} incorporation, according with the ICP analysis (low value of (Ca + Mg)/P). For Sr-HA, all Sr-substituted HA showed similar TG curves with pure HA. With a total weight loss ranging from 6.15 wt.% to 7.02 wt.%, the samples had no significant differences with each other. Similar to that of Mg-HA, the main weight loss of Sr-HA was ascribed to the adsorbed water and the decomposition of HPO_4^{2-}.

4. Discussion

A series of Mg- and Sr-substituted apatites were synthesized through a hydrothermal process. The XRD results, consistent with those of previous research

[14-15], indicated that the lattice parameters declined with the addition of Mg but increased with the addition of Sr. This finding can be attributed to the larger (smaller) atomic radius of Sr (Mg) than that of Ca. Actually, the previous studies have shown that the incorporation of ions, such as Mg^{2+}, Zn^{2+} and Co^{2+}, which are smaller than the ionic radius of Ca^{2+}, will decrease the lattice parameters [11, 23, 46]. On the contrary, bigger ions, like Sr^{2+} and Ba^{2+}, will increase the lattice parameters [12, 47]. Both the XRD and TEM analyses indicated that the crystallinity and crystal size decreased with the addition of Mg. In other words, the crystal growth of HA was inhibited by the presence of Mg^{2+}. Onuma et al. [48-49] studied the effect of Mg^{2+} and Zn^{2+} on the growth kinetics of a hydroxyapatite c-plane in pseudophysiological solutions and found that these ions inhibited the growth rate of the c-plane by absorbing at the kink sites of two-dimensional islands. Using hydrothermal method at 120 °C, Bigi et al. [50] studied the influence of Mg on HA crystallization. The result turned out that Mg inhibited the crystallization of HA by reducing the Ca/P molar ratio and crystal size of apatite. Meanwhile, it showed a threshold value of 35% to 50% Mg for crystallinity. The samples changed to the amorphous phase in meeting or exceeding this threshold value.

In this study, the value of (Ca + Mg)/P molar ratio declined sharply with the addition of Mg and decreased to a minimum value of 1.272 at a concentration of 50% Mg. It is well known that HA has the highest Ca/P molar ratio (1.67). When the Mg^{2+} was added, the Ca^{2+} cannot be fully substituted by Mg^{2+}. In addition, the HPO_4^{2-} group content increased with the addition of Mg^{2+} as indicated in Fig. 7. Some

previous studies [39, 51-52] reported that the weight of Mg substituted apatite declined sharply when they were treated at 500 °C to 700 °C. The incorporation of HPO_4^{2-} and weight loss may indicate that some defective HA formed during the Mg substitution. The formation of defective HA induced the sharply decline of the (Ca + Mg)/P molar ratio with the addition of Mg. Meanwhile, When the Mg content was more than 30% (below 40%), no diffraction peaks were found by X-ray diffraction, indicating the crystal disappear. (Suppl. Fig. S1). However, atoms with short-range ordering could still be observed at 50% Mg by the aid of HRTEM (Fig. 6 (c)). Previous studies show that the formation of HA was attributed to the correct arrangement of the $Ca_9(PO_4)_6$ cluster or octacalcium phosphate, both of which are the precursors of HA [53-54]. Furthermore, Onuma et al. [55] found that the growth mode of HA was multiple two-dimensional nucleation. Consequently, the growth of the a-plane was inhibited when the growth of the c-plane was inhibited by the absorbed Mg^{2+}. These atoms with short-range ordering were formed and could be the HA precursors or crystal nucleuses. Finally, these atoms with short-range ordering were wrapped by amorphous phosphate, as indicated by the elemental mapping presented in Fig. 5.

All Sr-substituted HA showed well crystallinity (decreased compared with pure HA, (Fig. 1, Table 1 and Suppl. Fig. S2)), but the addition of Sr may distort the crystal grain. The measured Sr contents were in good agreement with the designated Sr contents, as presented in Table 2, indicating the full substitution of Sr. The incorporation of larger ions Sr^{2+} into the crystal led to the greater distance of

Sr-hydroxyl than that of Ca-hydroxyl. Consequently, grain distortion and dislocation occurred after the substitution. Then, as the hexagonal structure was destroyed, the grains became more irregular. Unlike this experiment, a previous study, which used wet chemical method, showed that the crystallinity significantly decreased with the addition of Sr^{2+} up to 20% [38]. The results in the current study indicate that high temperature and pressure promote the Sr-substitution of HA.

According to the analysis results, the possible growth mechanism of HA with the substitution of Mg^{2+} and Sr^{2+} is shown in Fig. 8. For Mg^{2+}, when the content was low (~ 10%), a fraction of Mg^{2+} incorporated into the HA structure made the grain irregular and the remaining that was adsorbed on the surface of HA inhibited grain growth. The samples synthesized within this concentration range showed good crystallinity. With the increasing concentration of up to 30% Mg, both the Mg^{2+} incorporation and adsorption increased. On the one hand, the increased incorporation of Mg^{2+} made the grain more irregular. On the other hand, the adsorbed Mg^{2+} on the HA surface formed some dynamic Mg^{2+}-poor and Mg^{2+}-rich regions. The HA grains continued to grow in the Mg^{2+}-poor regions, but stopped growing in the Mg^{2+}-rich regions. As the two-dimensional growth progressed, the grain with a structure similar to a string of beads formed (20% Mg, see Suppl. Fig. S3). The size of the beads decreased with the increased Mg^{2+} until the nano-rods formed (30% Mg). Then, the fusiform cluster was formed by these nano-beads (or nano-rods) through the interaction of the adsorbed Mg^{2+}. The higher Mg^{2+}, the larger the size of the fusiform cluster was.

The ICP analysis showed a sudden increase in Mg content in Mg-HA from 3.8% for 10% Mg to 22.7% for 30% Mg. However, the positions of the diffraction peaks shifted differently from the previous study [14], indicating the existence of adsorbed Mg^{2+} in the clusters. When the Mg content was greater than 50%, the HA grain growth was inhibited by the adsorbed Mg^{2+} before it could completely form, resulting in atomic-scale ordering. The atomic-scale ordering was then wrapped by amorphous phosphate, forming the nano-hollow sphere agglomerates. Bigi et al. [56] prepared such nano-hollow sphere agglomerate structure by adjusting the Ca/P molar ratio to be equal to 2.55 via sol-gel method. However, its formation mechanism remains unclear. The further increase in Mg content of up to 60% ~ 80% led to the dimming of the corresponding SAED patterns, indicative of decreasing short-range ordering (see Suppl. Fig. S3) [57].

For Sr^{2+}, all the results demonstrated that Sr fully substituted the Ca, and formed $Ca_{10-x}Sr_x(PO_4)_6(OH)_2$ with good crystallinity (Fig. 1,Table 1 and Suppl. Fig. S2). The incorporation of Sr, which has a large atomic radius, caused lattice distortion, which destroyed the hexagonal structure and made the grain irregular. In this study, the lattice distortion degree increased with the addition of Sr and reached maximum at 50%. When the content exceeded 50%, the lattice distortion degree decreased with the Sr content until the grain exhibited a regular hexagonal structure again at 100%, at which the Ca was fully substituted by Sr and formed $Sr_{10}(PO_4)_6(OH)_2$ (Suppl. Fig. S4). It was worth noting that the aspect ratio increased visibly with the addition of Sr^{2+}. The samples completely became nano-rods with long c-axis at higher Sr^{2+}

concentration (90% ~ 100%), signifying an accelerated growth of the c-plane (Suppl. Fig. S4). The reason for this significant difference is still unclear, partially for atomic size or element electronegativity, and remains need for further study.

5. Conclusion

A series of Mg- and Sr-substituted HA was prepared by a conventional hydrothermal method and studied via various characterization techniques. The study revealed that the crystallinity, lattice parameter, grain size and thermostability decreased with increasing Mg fraction. The concentration for the transition from crystal to amorphous phase was between 30% and 40% Mg in this experiment. The incorporation of Sr did not change the thermostability, but increased the lattice parameter and slightly decreased the crystallinity. The mechanisms of the effects of Mg and Sr on HA are as follows: (I) a fraction of Mg for substitution and majority of Mg for adsorbing thus inhibited the grain growth. (II) Sr ions were fully incorporated into HA causing grain distortion and accelerating the c-plane growth. This study provides a certain reference, although the present condition is different from the in vivo situation.

Acknowledgements

This work was financially supported by National Natural Science Foundation of China (Grant No. 31200715, 31370970), Research Fund for the Doctoral Program of Higher Education of China (Grant No. 20120032120022).

References

[1] M. I. Kay, R.A. Young, A. S. Posner, Nature, 1964, **204**, 1050.

[2] M. Yoshinari, Y. Oda, T. Inoue, K. Matsuzaka, M. Shimono, Biomaterials, 2002, **23**, 2879.

[3] G. Darimont, R. Cloots, E. Heinen, L. Seidel, Legrand R., Biomaterials, 2002, **23**, 2569.

[4] M. Descamps, J.C. Hornez, A. Leriche, J. Eur. Ceram. Soc. 2009, **29**, 369.

[5] L.A. Grandjean, O. Tabary, J. Jacquot, D. Richard, P. Frayssinet, M. Guenounou, et al., Biomaterials, 2007, **28**, 400.

[6] E. While, E.C. Sors, Dent Clin North Am., 1986, **30**, 49.

[7] H.B. Wang, K. Jong, Moursi, J.J. Lannutti, J. Biomed. Mater. Res., 2003, **67**, 599.

[8] Z.L. Shi, X. Huang, Y.R. Cai, R.K. Tang, D.S. Yang, Acta Biomater., 2009, **5**, 338.

[9] B.S. Chang, C.K. Lee, K.S. Hong, H.J. Youn, H.S. Ryu, S.S. Chung, K.W. Park, Biomaterials, 2000, **21**, 1291.

[10] S. Kannan, J.H. Rocha, S. Agathopoulos, J.M. Ferreira, Acta Biomater., 2007, **3**, 243.

[11] F.Z. Ren, R.L. Xin, X. Ge, L. Yang, Acta Biomater., 2009, **5**, 3141.

[12] Z.L. Xiu, M.K. Lu, S.W. Liu, G.J. Zhou, B.Y. Su, H.P. Zhang, Mater. Res. Bull., 2005, **40**, 1617.

[13] V. Ljiljana, K. Ljiljana, S. Zoran, B. Ines, M. Smilja, I. Nenad, U. Dragan, J. Appl. Cryst., 2010, **43**, 320.

[14] W.L. Suchanek, K. Byrappa, P. Shuk, R.E. Riman, V.F. Janas, K.S. TenHuisen,

Biomaterials, 2004, **25**, 4647.

[15] P.G. Koutsoukos, G.H. Nancollas, J. Phys. Chem., 1981, **85**, 2403.

[16] F. Yang, D.Z. Yang, J. Tu, Q.X. Zheng, L.T. Cai, L.P. Wang, Stem Cells, 2011, **29**, 81.

[17] Z. Saidak, E. Hay, C. Marty, A. Barbara, J.M. Pierre, Aging Cell, 2012, **11**, 467.

[18] F. Barrere, C.A. van Blitterswijk, K. de Groot, P. Layrolle, Biomaterials, 2002, **23**, 2211.

[19] R.Z. Legeros, Calcium phosphates in oral biology and medicine, New York, Karger, 1991.

[20] E. Landi, A. Tampieri, B.M. Mattioli, G. Celotti, M. Sandri, A. Gigante, et al., J. Eur. Ceram. Soc., 2006, **26**, 2593.

[21] M. Percival, Appl. Nutr. Sci. Rep., 1999, **5**, 1.

[22] E. Landi, S. Sprio, M. Sandri, G. Celotti, A. Tampieri, Acta Biomater. 2008, **4**, 656.

[23] E. Landi, A. Tampieri, G. Celotti, S. Sprio, M. Sandri, G. Logroscino, Acta Biomater., 2007, **3**, 961.

[24] E. Gentleman, Y.C. Fredholm, G. Jell, N. Lotfibakhshaiesh, M.D. O'Donnell, R.G. Hill, et al., Biomaterials, 2010, **31**, 3949.

[25] M. Schumacher, A. Lode, A. Helth, M. Gelinsky, Acta Biomater., 2013, **9**, 9547.

[26] J. Braux, F. Velard, C. Guillaume, S. Bouthors, E. Jallot, J.M. Nedelec, D.L. Maquin, P. Laquerrière, Acta Biomater., 2011, **7**, 2593.

[27] C. Capuccini, P. Torricelli, F. Sima, E. Boanini, C. Ristoscu, B. Bracci, G. Socol,

M. Fini, I.N. Mihailescu, A. Bigi, Acta Biomater., 2008, **4**, 1885.

[28] K.L. Wong, C.T. Wong, W.C. Liu, H.B. Pan, M.K. Fong, W.M. Lam, W.L. Cheung, W.M. Tang, K.Y. Chiu, K.D.K. Luk, W.W. Lu, Biomaterials, 2009, **30**, 3810.

[29] B. Busse, B. Jobke, M. Hahn, M. Priemel, M. Niecke, S. Seitz, J. Zustin, J. Semler, M. Amling, Acta Biomater., 2010, **6**, 4513.

[30] J.Y. Reginster, E. Seeman, M.C. De Vernejoul, et al., J. Clin. Endocrinol. Metab. 2005, **90**, 2816.

[31] E. Seeman, B. Vellas, C. Benhamou, et al., J. Bone Miner. Res., 2006, **21**, 1113.

[32] G. Boivin, P. Deloffre, B. Perrat, G. Panczer, M. Boudeulle, Y. Mauras, et al., J. Bone Miner. Res., 1996, **11**, 1302.

[33] D. Farlay, G. Boivin, G. Panczer, A. Lalande, P.J. Meunier, J. Bone Miner. Res., 2005, **20**, 1569.

[34] P.N. Kumta, C. Sfeir, D.H. Lee, D. Olton, D. Choi, Acta Biomater., 2005, **1**, 65.

[35] D. Laurencin, A. Wong, J.V. Hanna, R. Dupree, M.E. Smith, J. Am. Chem. Soc., 2008, **130**, 2412.

[36] M.D. O'Donnell, Y. Fredholm, A. de Rouffignac, R.G. Hill, Acta Biomater., 2008, **4**, 1455.

[37] M. Kheradmandfard, M.H. Fathi. Ceram. Int., 2013, **39**, 1651.

[38] Z.Y. Li, W.M. Lam, C. Yang, B. Xu, G.X. Ni, S.A. Abbah, K.M.C. Cheung, K.D.K. Luk, W.W. Lu, Biomaterials, 2007, **28**, 1452.

[39] F. Ren, Y. Leng, R. Xin, X. Ge. Acta Biomater. 2010, **6**, 2787.

[40] D.G. Guo, Y.Z. Hao, H.Y. Li, C.Q. Fang, L.J. Sun, H. Zhu, J. Wang, X.F. Huang, P.F. Ni, K.W. Xu, J. Biomed. Mater. Res. Part B, 2013, **101B**, 1275.

[41] W.M. Lam, H.B. Pan, Z.Y. Li, C. Yang, W.K. Chan, C.T. Wong, K.D.K. Luk, W.W. Lu, Ceram. Int., 2010, **36**, 683.

[42] T.J. Webster, E.A. Massa-Schlueter, J.L. Smith, E.B. Slamovich, Biomaterials, 2004, **25**, 2111.

[43] E. Landi, A. Tampieri, G. Celotti, S. Sprio, J. Eur. Ceram. Soc., 2000, **20**, 2377.

[44] P. Habibovic, J.E. Barralet, Acta Biomater., 2011, **7**, 3013.

[45] J.C. Elliott, Structure and chemistry of the apatites and other calcium orthophosphates. Amsterdam, Elsevier, 1994.

[46] A. Bigi, G. Falini, E. Foresti, M. Gazzano, A. Ripamonti, N. Roveri, Acta Cryst., 1996, **52**, 87.

[47] L.C. Robert, J. Am. Chem. Soc., 1959, **81**, 5275.

[48] N. Kanzaki, K. Onuma, G. Treboux, S. Tsutsumi, A. Ito, J. Phys. Chem. B, 2000, **104**, 4189.

[49] N. Kanzaki, K. Onuma, G. Treboux, S. Tsutsumi, A. Ito, J. Phys. Chem. B, 2001, **105**, 1991.

[50] A. Bigi, G. Falini, E. Foresti, A. Ripamonti. J. Inorg. Biochem., 1993, **49**, 69.

[51] B. Uma, K. Seema, S. Sonia, J. Mater. Eng. Perform., 2013, **22**, 1798.

[52] Z. Yang, Y. Jiang, L.X. Yu, B. Wen, F. Li, S. Sun, T. Hou, J. Mate. Chem., 2005, **15**, 1807.

[53] W. E. Brown, J. P. Smith, J.R. Lehr, A.W. Frazier, Nature, 1962, **196**, 1048.

[54] K. Onuma. A. Ito, Chem. Mater., 1998, **10**, 3346.

[55] N. Kanzaki, K. Onuma, A. Ito, K. Teraoka, T. Tateishi, S. Tsutsumi, J. Phys. Chem. B, 1998, **102**, 6471.

[56] A. Bigi, E. Boanini, K. Rubini, J. Solid State Chem., 2004, **177**, 3092.

[57] Q. Wang, C.T. Liu, Y. Yang, Y.D. Dong, J. Lu, Phys. Rev. Lett., 2011, **106**, 215505.

Figure captions

Fig. 1. XRD patterns of as-prepared Mg- and Sr-substituted HA powders.

Fig. 2. FT-IR spectra of prepared Mg- and Sr-substituted HA powders.

Fig. 3. SEM images of the synthesized samples: (a) 10% Mg, (b) 30% Mg, (c) 50% Mg, (d) 10% Sr, (e) 30% Sr, and (f) 50% Sr. Scale bars: 200nm.

Fig. 4. TEM and SAED patterns of the synthesized samples: (a) pure HA, (b) HRTEM of pure HA, (c) 10% Mg, (d) 10% Sr, (e) 30% Mg, (f) 30% Sr, (g) 50% Mg, and (h) 50% Sr. Scale bars: a and c-h, 100nm; b, 5nm.

Fig. 5. Elemental mapping of the 50% Mg sample.

Fig. 6. HRTEM images of the synthesized samples: (a) 10% Mg, (b) 30% Mg, (c) 50% Mg, (d) 10% Sr, (e) 30% Sr, and (f) 50% Sr. Scale bars: 5nm.

Fig. 7. TG curves of the prepared samples. The inset shows the details of some curves.

Fig. 8. Schematics of the effects of Mg^{2+} and Sr^{2+} on the growth mechanism of HA.

Table 1. Lattice parameters and crystallinity of the prepared samples.

Table 2. ICP measured elemental composition of the synthesized samples.

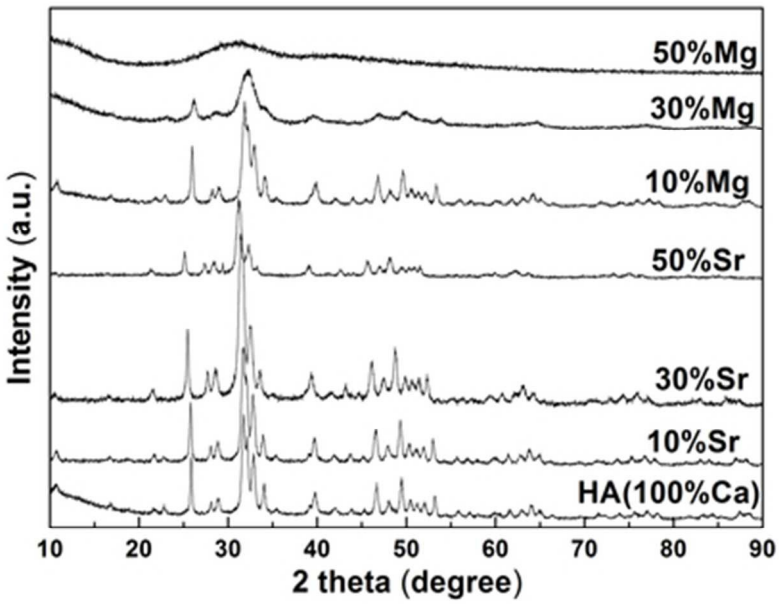

XRD patterns of as-prepared Mg- and Sr-substituted HA powders.
22x15mm (600 x 600 DPI)

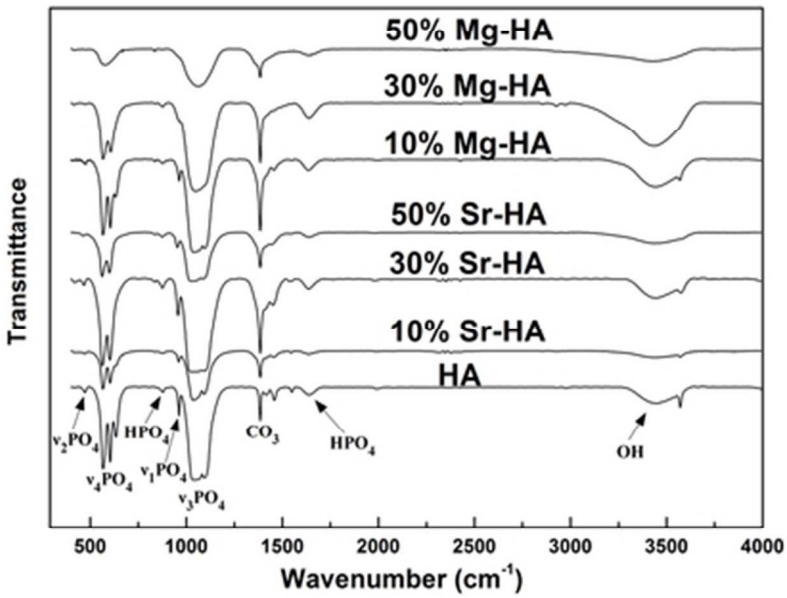

FT-IR spectra of prepared Mg- and Sr-substituted HA powders.
22x15mm (600 x 600 DPI)

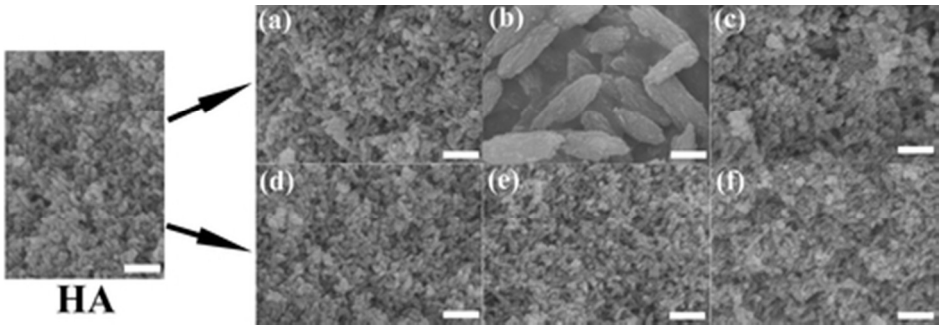

SEM images of the synthesized samples: (a) 10% Mg, (b) 30% Mg, (c) 50% Mg, (d) 10% Sr, (e) 30% Sr, and (f) 50% Sr. Scale bars: 200nm.
19x6mm (600 x 600 DPI)

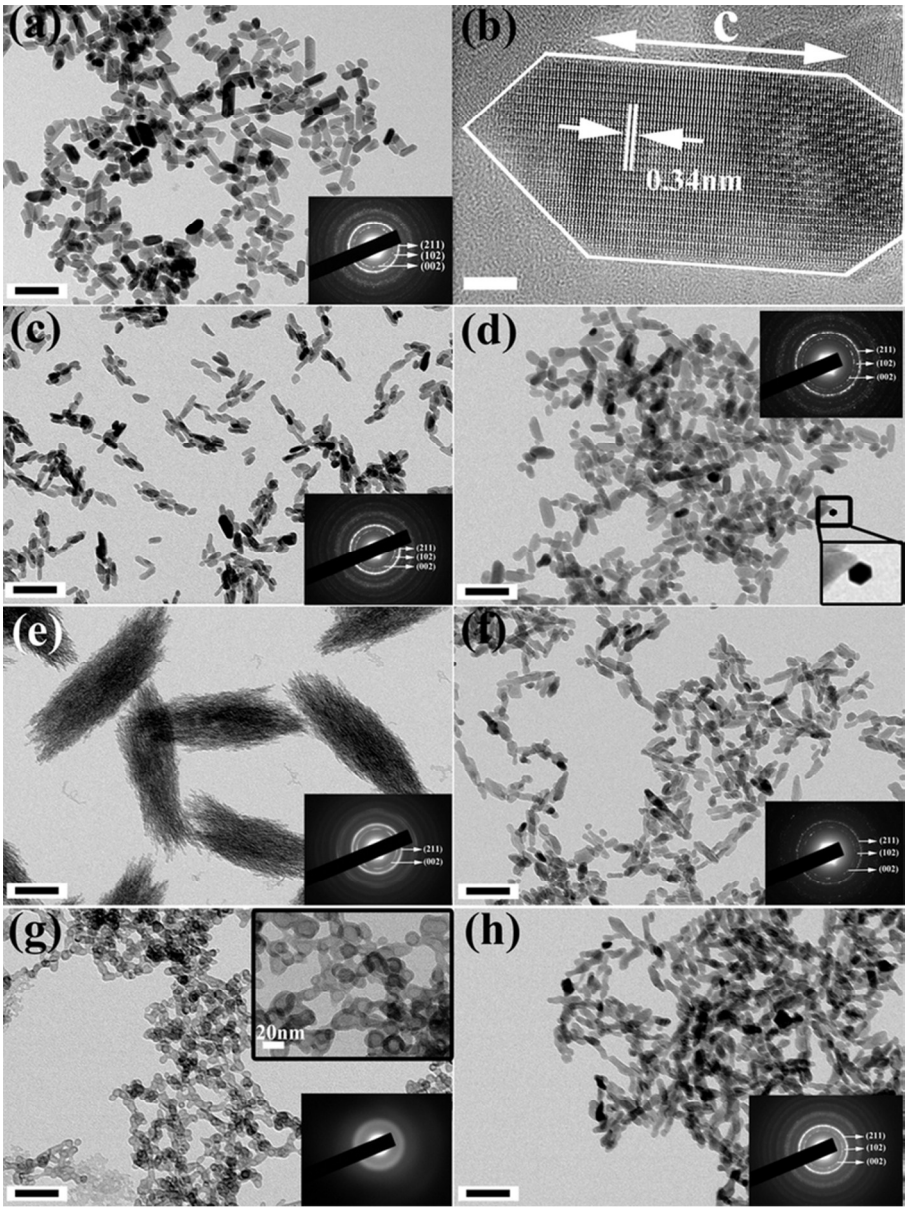

TEM and SAED patterns of the synthesized samples: (a) pure HA, (b) HRTEM of pure HA, (c) 10% Mg, (d) 10% Sr, (e) 30% Mg, (f) 30% Sr, (g) 50% Mg, and (h) 50% Sr. Scale bars: a and c-h, 100nm; b, 5nm.
67x90mm (300 x 300 DPI)

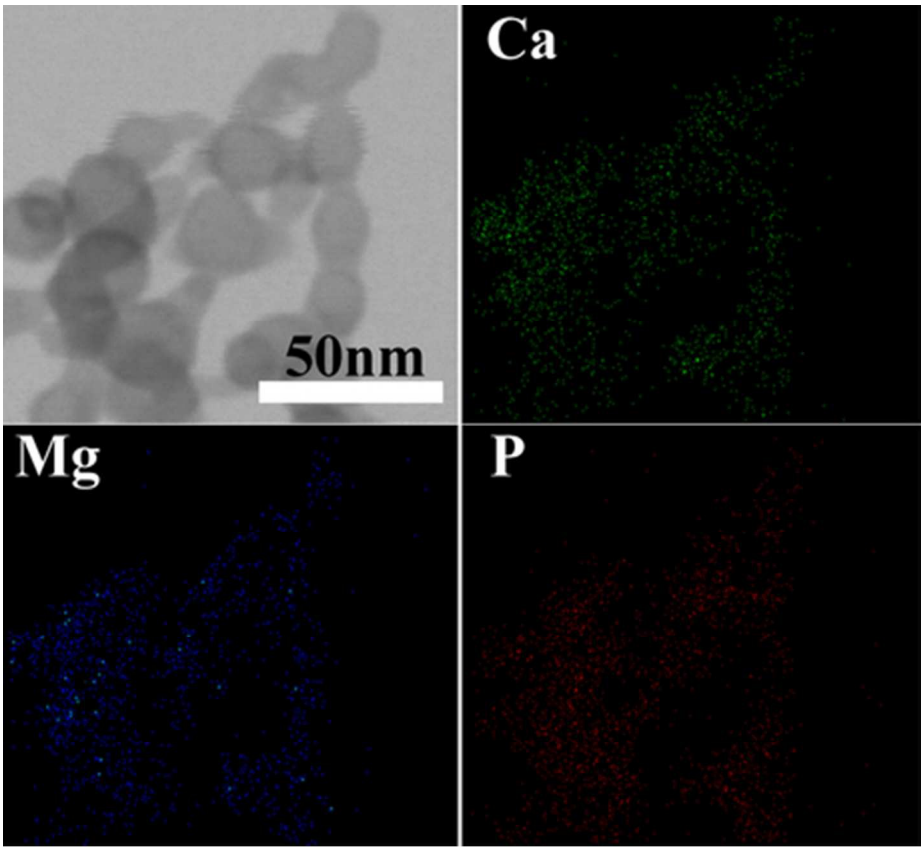

Elemental mapping of the 50% Mg sample.
19x17mm (600 x 600 DPI)

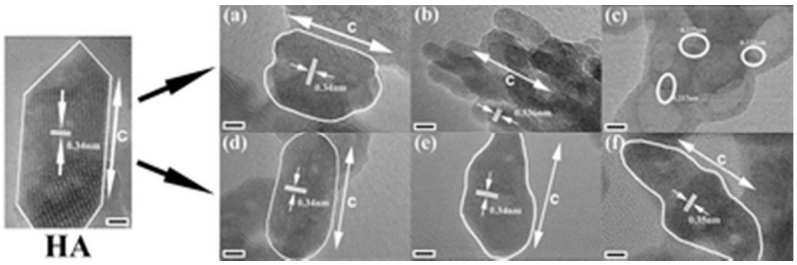

HRTEM images of the synthesized samples: (a) 10% Mg, (b) 30% Mg, (c) 50% Mg, (d) 10% Sr, (e) 30% Sr, and (f) 50% Sr. Scale bars: 5nm.
16x5mm (600 x 600 DPI)

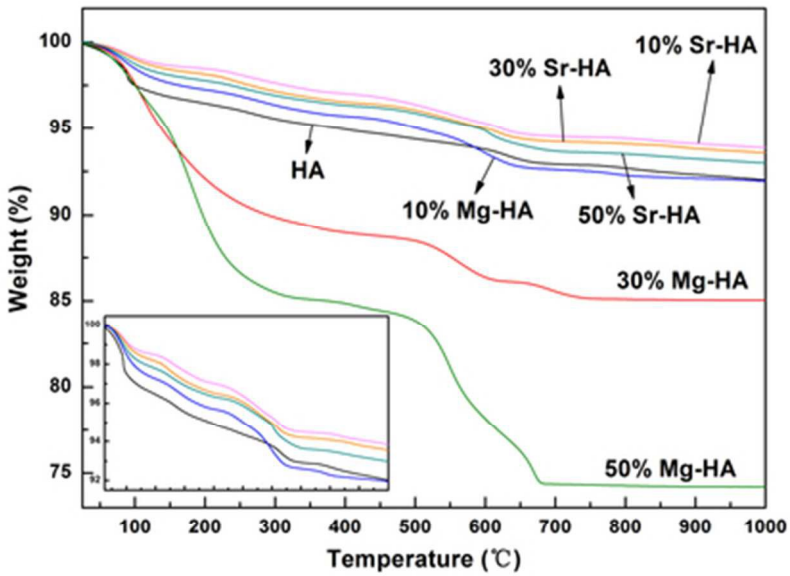

TG curves of the prepared samples. The inset shows the details of some curves.
22x15mm (600 x 600 DPI)

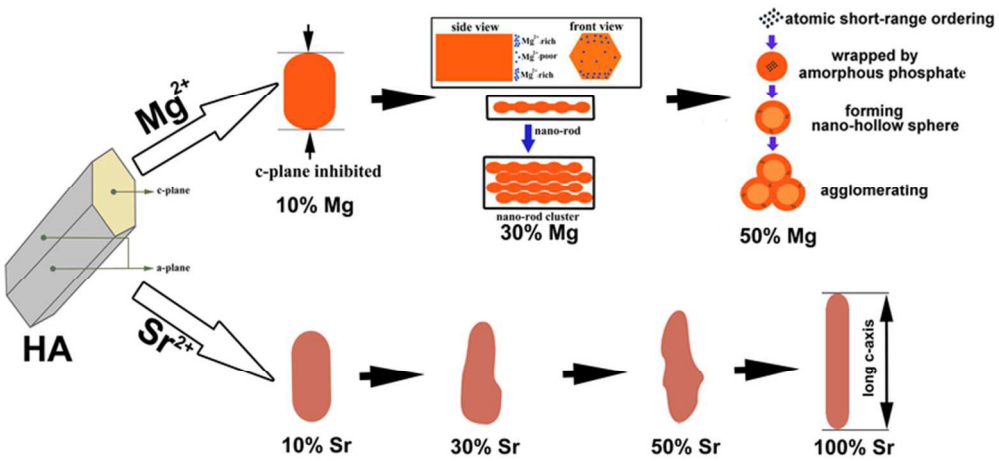

The hydroxyapatite crystals grow in different ways when the calcium is substituted by strontium or magnesium.

Schematics of the effects of Mg2+ and Sr2+ on the growth mechanism of HA.
35x19mm (600 x 600 DPI)

Table 1

Samples	Crystallinity	**2θ** values of (002)	Lattice parameters	
			a axis (Å)	**c** axis (Å)
HA	54.9%	25.855	9.4035	6.8692
10% Mg	34.8%	25.958	9.3892	6.8380
30% Mg	4.5%	26.183	9.3041	6.7743
50% Mg	0		—	—
10% Sr	54.5%	25.814	9.4522	6.9103
30% Sr	42.4%	25.486	9.5138	6.9879
50% Sr	39.0%	25.219	9.5613	7.0712

Table 2

Designed sample	Measured concentration								
	Ca(mol.%)	Mg(mol.%)	Sr(mol.%)	P(mol.%)	Mg:(Ca+Mg)	Sr:(Ca+Sr)	(Ca+Mg):P	(Ca+Sr):P	Ca:P
HA	62.14 ± 0.37	—	0.06 ± 0.01	37.80 ± 0.35	——	——	——	——	1.643 ± 0.03
10%Mg	58.88 ± 1.05	2.34 ± 0.09	0.07 ± 0.03	38.71 ± 1.07	0.038 ± 0.001	——	1.583 ± 0.07	——	1.522 ± 0.07
30%Mg	45.04 ± 0.38	12.01 ± 0.58	0.03 ± 0.01	42.92 ± 0.82	0.227 ± 0.02	——	1.330 ± 0.04	——	1.05 ± 0.03
50%Mg	33.89 ± 1.16	22.06 ± 2.15	0.05 ± 0.005	44.00 ± 1.00	0.394 ± 0.03	——	1.272 ± 0.05	——	0.77 ± 0.01
10%Sr	57.49 ± 0.47	—	5.10 ± 0.28	37.41 ± 0.27	——	0.081 ± 0.004	——	1.674 ± 0.02	1.537 ± 0.02
30%Sr	44.54 ± 0.57	—	17.69 ± 0.60	37.77 ± 0.13	——	0.284 ± 0.009	——	1.647 ± 0.009	1.179 ± 0.02
50%Sr	29.84 ± 0.33	—	32.47 ± 0.65	37.69 ± 0.38	——	0.52 ± 0.008	——	1.653 ± 0.027	0.792 ± 0.008

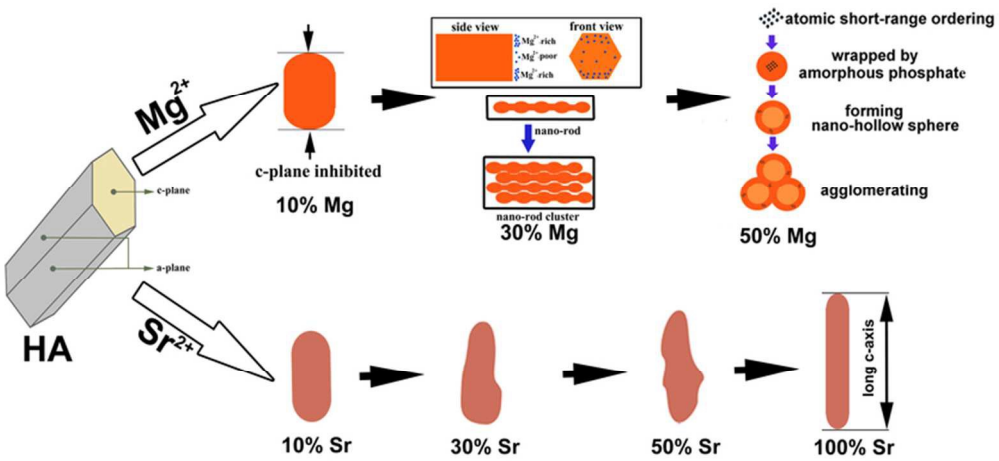

The hydroxyapatite crystals grow in different ways when the calcium is substituted by strontium or magnesium.

Graphical Abstract

35x19mm (600 x 600 DPI)